S40RTS: a degree-40 shear-velocity model for the mantle from new Rayleigh wave dispersion, teleseismic traveltime and normal-mode splitting function measurements

J. Ritsema,[1] A. Deuss,[2] H. J. van Heijst[3] and J. H. Woodhouse[3]

[1]*Department of Geological Sciences, University of Michigan, Ann Arbor MI 48109, USA. E-mail: jritsema@umich.edu*
[2]*Bullard Labs, Department of Earth Sciences, University of Cambridge, Cambridge CB3 0EZ, UK*
[3]*Department of Earth Sciences, University of Oxford, Oxford OX1 3PR, UK*

SUMMARY

We have developed model S40RTS of shear-velocity variation in Earth's mantle using a new collection of Rayleigh wave phase velocity, teleseismic body-wave traveltime and normal-mode splitting function measurements. This data set is an order of magnitude larger than used for S20RTS and includes new data types. The data are related to shear-velocity perturbations from the (anisotropic) PREM model via kernel functions and ray paths that are computed using PREM. Contributions to phase delays and traveltimes from the heterogeneous crust are estimated using model CRUST2.0. We calculate crustal traveltimes from long-period synthetic waveforms rather than using ray theory. Shear-velocity perturbations are parametrized by spherical harmonics up to degree 40 and by 21 vertical spline functions for a total of 35 301 degrees of freedom. S40RTS is characterised by 8000 resolved unknowns. Since we compute the exact inverse, it is straightforward to determine models associated with fewer or more unknowns by adjusting the model damping. S40RTS shares many characteristics with S20RTS because it is based on the same data types and similar modelling procedures. However, S40RTS shows more clearly than S20RTS the abrupt change in the pattern of shear-velocity heterogeneity across the 660-km phase transition and it presents a more complex patern of shear-velocity heterogeneity in the lower mantle. Utilities to visualise S40RTS and software to analyse the resolution of S40RTS (or models for different damping parameters) are made available.

Key words: Composition of the mantle; Body waves; Surface waves and free oscillations; Seismic tomography.
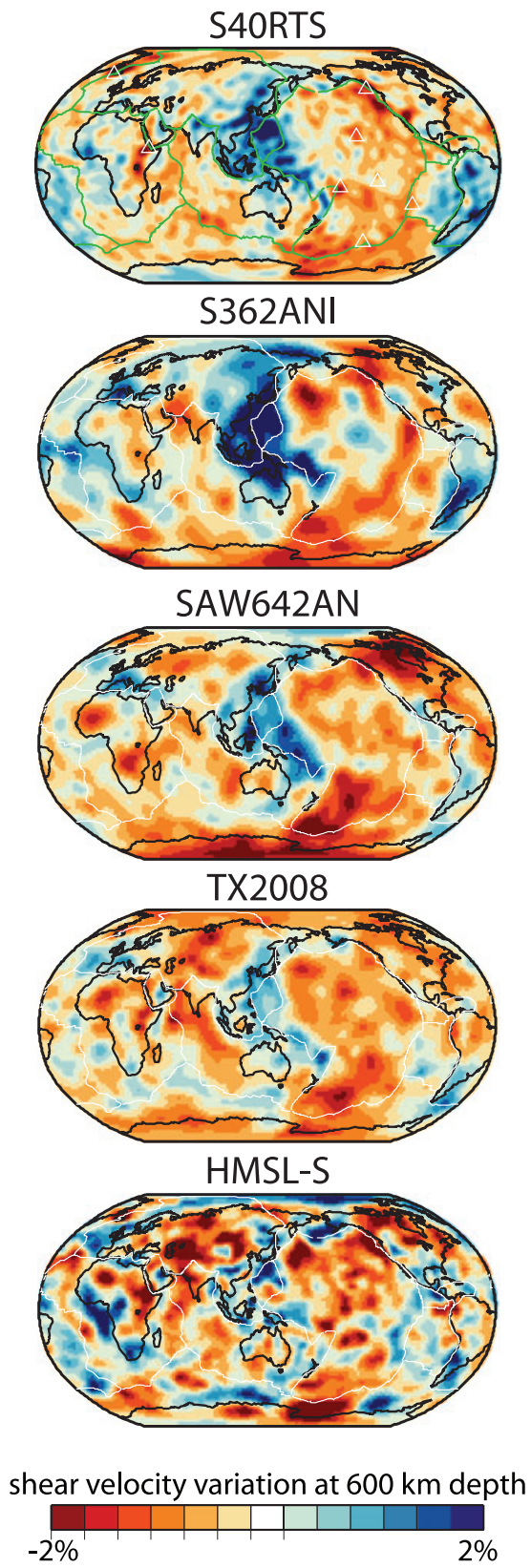
GJI Seismology

1 INTRODUCTION

Seismic tomography is one of the most important tools for elucidating the a-spherical (3-D) structure of Earth's mantle. Since the earliest seismic models of the mantle have been developed (e.g. Dziewonski *et al.* 1977; Woodhouse & Dziewonski 1984), they have been key input in the geophysical interpretation of the geoid, topography, hotspot volcanism and large-scale mantle dynamics (e.g. Hager *et al.* 1985; Hager & Richards 1989; Richards & Engebretson 1992; Ricard *et al.* 1993). See Becker & Boschi (2002) and Romanowicz (2003) for reviews.

Apart from well-sampled subduction zone regions (van der Hilst *et al.* 1991; Fukao *et al.* 1992), it has remained difficult to place global constraints on the seismic structure of the transition zone and lower mantle above D″. Here, seismic heterogeneity is relatively weak and small in scale. Moreover, overtone surface waves and multiple shear-wave reflections, ideal seismic signals for studying the transition zone, are excited primarily by relatively strong

($M_W > 7$) earthquakes at intermediate depths ($H > 50$ km) and their waveforms are complex due to wave interactions with the free surface and lithosphere.

Fig. 1 shows six maps of the shear-velocity structure at a depth of 600 km according to models from six independent research groups: S40RTS (this study), S362ANI (Kustowski *et al.* 2008), SAW642AN (Panning & Romanowicz 2006), TX2008 (Simmons *et al.* 2009) and HMSL-S (Houser *et al.* 2008). Taken at face value, the maps display significant differences even if we consider the continental-scale (∼4000 km) velocity variations. Note, for example, the variable strengths of high-velocity anomalies beneath the western Pacific subduction zones and the variable widths of low-velocity anomalies beneath oceans and continents. While the transition zone may separate vigorous convection in the upper mantle and sluggish convection in the lower mantle, it is difficult to infer the role of the 660-km phase and viscosity transition on large-scale material flow and plume ascent on the basis of Fig. 1. It is necessary to improve models of the transition zone and lower mantle by maximising

S40RTS

S362ANI

SAW642AN

TX2008

HMSL-S

shear velocity variation at 600 km depth

-2%   2%

Figure 1. Comparison of shear-velocity maps at a depth of 600 km for models (from top to bottom) S40RTS (this study), S362ANI (Kustowski *et al.* 2008), SAW642AN (Panning & Romanowicz 2006), TX2008 (Simmons *et al.* 2009) and HMSL-S (Houser *et al.* 2008). The velocity varies from −2 per cent to +2 per cent from the average value.

data coverage. In addition, geophysical interpretations must rely on quantitative analyses of resolution to facilitate model comparison and to recognise artefacts.

In this paper, we describe a new model of shear-velocity variations in the mantle. This model, S40RTS, is a successor to S20RTS described by Ritsema *et al.* (1999) (RHW99 from hereon) and Ritsema *et al.* (2004) (RHW04 from hereon). The effort in developing S40RTS has focused on maximising data coverage of the mantle. It is well-known that seismic wave sampling of the deep mantle is heterogeneous because most earthquakes occur in narrow belts along plate boundaries and seismometers are primarily installed on land (e.g. Wysession 1996). Until it becomes practical to extend instrumental coverage into the oceans (e.g. Simons *et al.* 2009), we must exploit the rich information in seismograms to overcome the limited earthquake and seismic station distribution. In principle, it is possible to relate any portion of the seismogram to seismic structure via adjoint methods (Liu & Tromp 2006, 2008). However, we follow here a classical approach in which nearly all high-amplitude signals in seismograms are identified as body-wave or surface-wave phases or normal-mode spectral peaks and analysed via waveform modeling.

The parametrization of the mantle and the modelling strategies used in S20RTS and S40RTS are very similar. Waveform anomalies (e.g. traveltime delays, phase delays and normal-mode splitting) are identified using Preliminary Reference Earth Model (PREM) (Dziewonski & Anderson 1981) synthetics and related to 3-D shear-velocity heterogeneity with ray paths and sensitivity kernels computed using PREM. Thus, S40RTS is a model of 3-D perturbations of isotropic shear velocity with respect to the PREM model. We invert the data using a damped least-squares inversion scheme. By computing the inverse of the G^TG matrix, it is straightforward to investigate models of shear velocity for any dampings factor and to determine the accompanying model resolution matrices.

We focus on presenting S40RTS and leave detailed image interpretations for forthcoming studies. In Section 2, we describe the data sets used in S40RTS is some detail. We discuss the modelling procedures in Section 3, including a brief discussion of finite-frequency crustal corrections, the forward modelling approach and model parametrization. We describe S40RTS in Section 4 and compare it to other recently published global shear-velocity models in Section 5.

2 DATA

Akin to RHW99 and RHW04 we use three data types: Rayleigh-wave phase delays, traveltimes of teleseismic body waves and the splitting functions of normal modes. These data provide complementary constraints on the shear-velocity structure of the mantle. The upper third of the mantle is primarily constrained by Rayleigh-wave dispersion and the lower two thirds of the mantle are constrained by teleseismic traveltimes. Whole-mantle constraints, especially at the longest wavelengths, are obtained from normal-mode splitting functions. We have updated the waveform collection with seismograms from 2003–2008, analysed new body-wave phases and measured the splitting functions using the most recent earthquakes with moment magnitudes of 7.4 and higher. The data set is roughly 10 times larger than the data set used by RHW99.

2.1 Rayleigh wave phase velocities

We have used the mode-branch-stripping technique of van Heijst & Woodhouse (1997) to measure the dispersion of the fundamental

Table 1. Phase velocity measurements (misfit at $T = 62$ s).

	Minor arcs			Major arcs		
Branch	Period (s)	Number	Misfit	Period (s)	Number	Misfit
Fund. mode	275–40	18,304,840	0.07	275–40	2 469 534	0.09
1st overtone	235–40	988,459	0.21	200–69	511 013	0.66
2nd overtone	114–40	909,654	0.20	131–62	638 492	0.40
3rd overtone	100–43	844,067	0.38	69–51	498 594	0.52
4th overtone	62–40	817,414	0.31	56–46	633 791	–

and first four overtone Rayleigh waves. In contrast to full wave-form modelling techniques, this technique allows us to measure the dispersion of overlapping overtone branches and to treat them as independent data with relatively high weights. As demonstrated in RHW04, the overtone Rayleigh-wave data are important for imaging the transition zone because they are sensitive to velocity variations well below 400 km depth. Moreover, overtone surface waves sample the transition zone much better than teleseismic body waves especially beneath poorly instrumented regions like the oceans.

The data set has been extended to include measurements for all earthquakes from the Global CMT catalog up to 2008 (Table 1). It includes over 20 million phase-velocity measurements for minor-arc and major-arc paths and they are derived from both vertical and horizontal-component long-period seismograms. The misfit (which includes misfit reduction by CRUST2.0) is lower than 10 per cent for the fundamental-mode Rayleigh-waves. Misfit is relatively high for the overtone Rayleigh waves because shear-velocity variations below a depth of 200 km of the mantle are relatively weak and the effects of the crust are smaller.

We refer the readers to van Heijst & Woodhouse (1997) for details on the overtone measurements and incorporated reliability estimates, to van Heijst & Woodhouse (1999) for a discussion of overtone phase-velocity maps, to RHW04 for the inversion for shear-velocity structure in the mantle and to Trampert & van Heijst (2002) for a discussion of azimuthal anisotropy in the transition zone based on our overtone measurements.

2.2 Teleseismic traveltimes

We use the procedure of Ritsema & van Heijst (2002) to measure traveltime anomalies of distinct body-wave phases with respect to PREM. This procedure involves a cross-correlation of low-pass filtered seismogram and synthetics (computed for PREM and CMT source parameters) within 80-s wide time windows around major body-wave phases. Automated checks ensure that the window includes only one high-amplitude body-wave phase. The quality of the measurements is quantified from measurements of noise, waveform fit, wave amplitude discrepancies and the amplitude of body-wave coda.

Our data set includes 500 000 traveltime measurements (Table 2). In addition to *SKS* and *SKKS*, which are recorded on radial component seismograms, we have updated the set of traveltimes for *S* (and S_{diff}), *SS* and *SSS* measured on transverse component seismograms.

We have expanded the collection of traveltimes of multiple core reflections (e.g. ScS_2, ScS_3, ScS_4) and surface reflections (e.g. *SS*, *SSS*) by expanding the epicentral distance range. Multiple core reflections are well recorded up to an epicentral distance of 110°. They have up to eight propagation segments in the mantle and traverse the lower mantle more steeply than *S, SS,* and *SSS*.

The traveltimes of multiple surface reflections that have propagated along the major great-circle arc (e.g. SS_{M}, SSS_{M}, $SSSS_{\text{M}}$)

Table 2. Traveltime measurements.

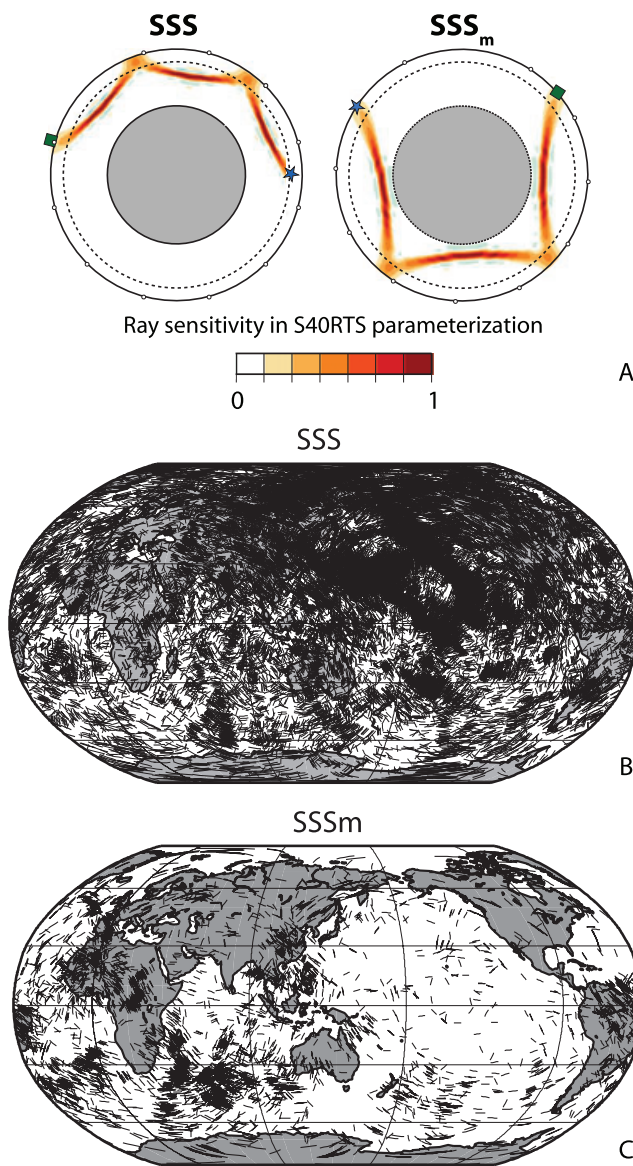| Phase	Number	Misfit
S, S_{diff}	194 488	0.23
SS	125 068	0.16
SSS	28 288	0.17
SKS	35 267	0.47
$SKKS$	9 183	0.51
ScS, $sScS$	10 329	0.34
ScS_2, ScS_3, ScS_4	28 200	0.21
SS_m, SSS_m, $SSSS_m$	28 690	0.25

between distances of about 245°–280° are new data. Although their ray geometries are similar to *SS, SSS* and *SSSS* (Fig. 2a), major-arc surface reflections sample different regions since they propagate in the opposite direction. Figs 2(b) and (c) compare the upper mantle sampling of the minor-arc *SSS* phase to the sampling of the major-arc SSS_{M}. Since most seismic stations are in the northern hemisphere, SSS reflects off the surface primarily in the northern hemisphere. On the other hand, most of the SSS_{M} surface reflection points are within the southern oceans where the *SSS* sampling is relatively poor.

The multiple core reflections and major-arc surface reflections have relatively small amplitudes due to their long propagation paths. In practise, most traveltimes of these phases are obtained for deep earthquakes with moment magnitudes larger than about 7 when these phases are not obscured by the short-period Love-wave train. Our data set include 28 200 ScS_2, ScS_3, ScS_4 traveltimes and 28 690 SS_{M}, SSS_{M} and $SSSS_{\text{M}}$ traveltimes. Combined, these traveltimes represent about 10 per cent of the total number of traveltimes. We note, however, that 57 000 traveltime measurements is a significant set when compared to traveltime collections from the 1990s.

For all phases we also measure the traveltime of accompanying depth phases (e.g. $sSKS$, sSS, $s ScS_3$) if earthquakes are deeper than 150 km. Misfit is lowest for body waves that have multiple segments through the heterogeneous upper mantle (e.g. *SS* and *SSS*).

2.3 Splitting functions

Normal modes provide important constraints on the longest wavelength structure in the mantle (Fig. 3). In RHW99 and RHW04 we used the splitting function data up to 3 mHz from Resovsky & Ritzwoller (1999). The new data set has been entirely reprocessed because a number of large events have occurred since the most recent compilation of normal-mode splitting functions. Our new data set contains modal spectra up to 3 mHz for all $M_{\text{W}} > 7.6$ events from the last 32 years (1976–2008) and all $M_{\text{W}} > 7.4$ earthquakes deeper than 100 km. In particular, we now have continental earthquakes (including the 2008 M_{W} 7.9 Wenchuan China, 1999 M_{W} 7.6 Turkey and 2005 M_{W} 7.6 Pakistan events) in addition to subduction zone earthquakes. The new data set also includes the

Figure 2. (a) Ray paths for the phases (left) *SSS* and (right) *SSS*ₘ projected into the S40RTS parametrization. Maps (b) and (c) show the projections (black lines) of 4°-long segments of geometrical rays at the surface reflection points of *SSS* and *SSS*ₘ, respectively.

2004 December 26 Sumatra event and its 2005 March 25 aftershock.

A total of 92 new events provide significant increase of data coverage in previously under-sampled regions. Our data set includes splitting functions of 49 spheroidal modes of the fundamental branch and the first five overtones derived from over 84 000 spectral–spectral measurements (Table 3). We exclude several 5th overtone modes with large sensitivity to *P* velocity. In addition, we exclude inner-core sensitive modes, which are strongly split due to inner-core anisotropy (Woodhouse *et al.* 1986).

The splitting functions are measured from normal-mode spectra using the approach of Resovsky & Ritzwoller (1999). We allowed for cross-coupling between pairs of modes which are close in frequency. We only use the even-degree self-coupling splitting functions in our S40RTS inversion. The inversions for splitting functions were started from PREM; we were able to obtain good convergence

without starting from a 3-D mantle model. Error bounds were determined using cross-validation.

As our data set is significantly larger than the older data sets, we were able to measure splitting functions with a higher precision than was possible before. For example, mode $_2S_{12}$, which is strongly sensitive to shear velocity in the upper mantle, was measured using 2668 spectral peaks (a ten-fold increase compared to previous data sets) and we measured its splitting function up to angular order 20. The splitting data set will be discussed further by Deuss *et al.* (2010).

3 MODELLING PROCEDURE

We follow closely the modelling procedure of RHW04 but note here several important modifications.
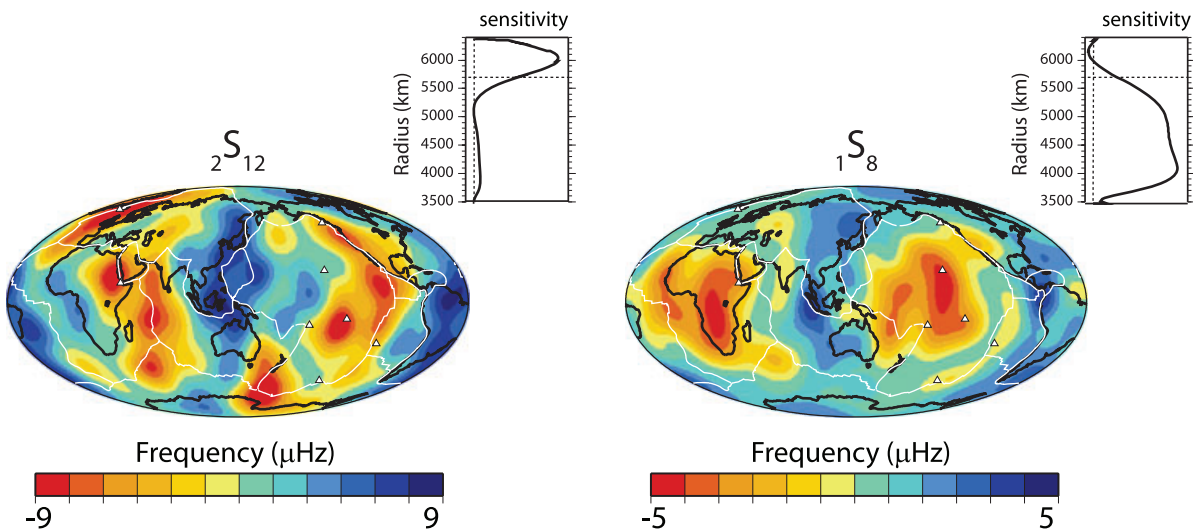
3.1 Isotropic *S* velocity inversion

S40RTS is a model of isotropic shear-velocity perturbations from PREM. The shear-velocity structure has a first-order effect on traveltimes, normal-mode splitting and surface-wave dispersion. Although there is abundant evidence for the presence of seismic anisotropy in the mantle, we ignore anisotropy in our model in contrast to recent work by Ekström & Dziewonski (1998), Debayle *et al.* (2004), Panning & Romanowicz (2006), Kustowski *et al.* (2008) (see also the sreviews by Montagner 1998, 2007). Only modest additional misfit reduction can be attained when variable anisotropy is incorporated in global models (e.g. Panning & Romanowicz 2006). Moreover, the resolution of anisotropy in the mantle is further complicated by the uncertain effects of the crust on surface-wave dispersion (e.g. Bozdağ & Trampert 2008; Feirrera *et al.* 2010).

We have experimented with inversions in which *P*-velocity variations are included in the upper 300 km of the mantle. The addition of *P*-velocity variations helps to reduce the misfit of the long-period surface waves and explains qualitatively the ocean-continent pattern of *PP* traveltimes seen by Ritsema & van Heijst (2002). However, it has no effect on the resolution of shear velocity. A more complete analysis of the long-wavelength P structure from splitting functions and *P* wave traveltimes will be presented in a forthcoming paper.

We calculate the sensitivity of splitting functions and Rayleigh-wave dispersion to velocity variations using PREM. We assume a constant scaling between shear velocity and density ($\delta \ln \rho / \delta \ln V_S = 0.5$) and we assume that the scaling between shear velocity and *P* velocity ($\delta \ln V_S / \delta \ln V_P$) increases from 2 at the surface to 3 at the core–mantle boundary. This scaling provides optimal fit to teleseismic *P* wave traveltimes and *P*-sensitive splitting functions.

3.2 Ray-based propagation paths

Apart from describing the effects of diffraction of waves with finite wavelengths, new theoretical approaches allow us to invoke volumetric rather than ray-based, sensitivity kernels for body waves (Dahlen *et al.* 2000; Nolet & Dahen 2000; Zhao *et al.* 2000) and surface waves (Li & Romanowicz 1995; Marquering *et al.* 1996; Yoshizawa & Kennett 2002). Indeed, several authors have measured body-wave traveltimes at multiple frequencies and use the frequency-dependence of the sensitivity kernels to improve tomographic inversions (Montelli *et al.* 2004; Sigloch

© 2010 The Authors, *GJI*, **184,** 1223–1236
Geophysical Journal International © 2010 RAS

Figure 3. Splitting functions for modes (left) $_2S_{12}$ and (right) $_1S_8$ which are sensitive to shear-velocity structure in the upper mantle and lower mantle, respectively. Shear wave sensitivity kernels of these modes are shown to the upper-right.

Table 3. Splitting function measurements.

Modes	# spectra	Misfit
$_0S_3-_0S_{21}$	30 544	0.13
$_1S_2-_1S_{10}, _1S_{14}$	11 731	0.16
$_2S_4-_2S_{13}$	19 404	0.08
$_3S_6-_3S_9$	6 812	0.17
$_4S_1-_4S_5$	9 700	0.16
$_5S_3-_5S_6$	5 849	0.23

et al. 2008; Zaroli *et al.* 2010). Obviously, finite-frequency kernels describe the sensitivity of waves better than kernels based on ray-theory, especially when they are calculated for 3-D models (Chen *et al.* 2007; Fichtner *et al.* 2009; Tape *et al.* 2009). However, we apply ray-theory and the great-circle approximation to describe the propagation of body waves and surface waves. As in RHW99 and RHW04 (see also Kustowski *et al.* (2008)) we relate phase-velocity anomalies, traveltime anomalies and splitting functions to shear-velocity heterogeneity by assuming that the Rayleigh wave is affected by structure in the plane of propagation, that the traveltime is affected by velocity heterogeneity along the geometrical ray and that splitting functions can be mapped into velocity heterogeneity using depth-dependent kernel functions. Ray theory is easily implemented and it is our view that the geophysical interpretations of models based on ray-theory and finite-frequency theory are, in essence, the same.

Montelli *et al.* (2004) show that there is a difference in the resolved amplitude of velocity anomalies if finite-frequency theory is used in body-wave tomography. However, they also demonstrate that maps derived from traveltime inversion using ray theory and finite-frequency theory correlate nearly perfectly. In Fig. 4, we compare fundamental-mode Rayleigh phase-velocity maps at periods of 50 s and 100 s that are derived with ray theory and with finite-frequency theory following Spetzler *et al.* (2002). Rayleigh waves at these periods are strongly sensitive to the crust and lithosphere where velocity heterogeneity is strong. Although these maps are derived using different amounts of damping, all maps are characterised by 1350 effective unknowns. The minor differences between the maps demonstrate that virtually identical structure can be derived from the great-circle approximation and finite-frequency theory if the regu-

larisation is adjusted. This has previously been demonstrated by Trampert & Spetzler (2006). For additional discussion, see Boschi (2003), van der Hilst & de Hoop (2005), Montelli *et al.* (2006) and Trampert & Spetzler (2006).
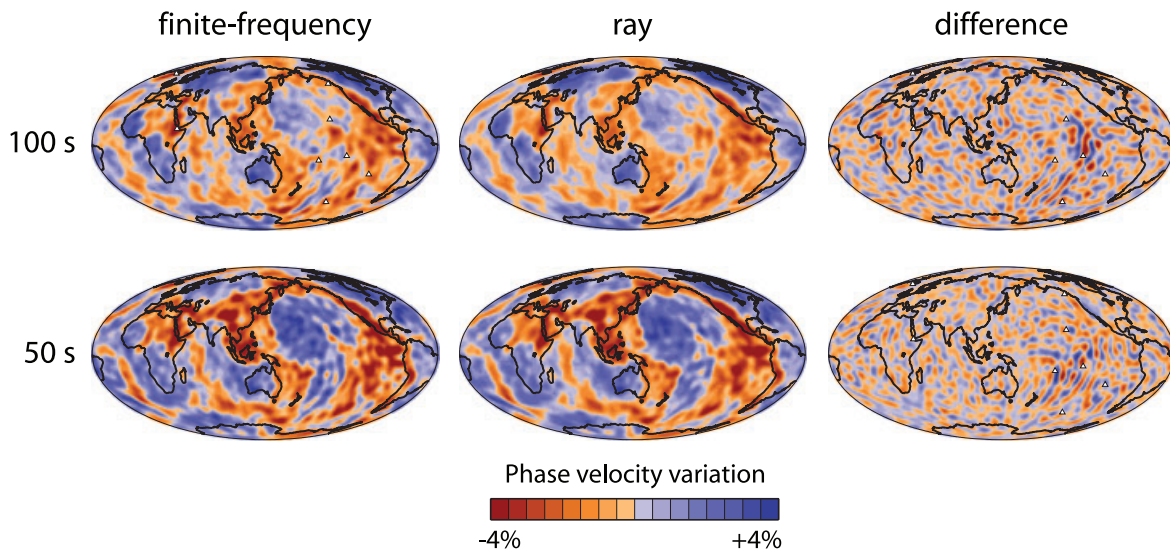
3.3 Crustal corrections

The crust has a profound influence on traveltimes. We make a-priori crustal corrections by subtracting the contribution to the Rayleigh-wave phase delay due to the crust. We correct the Rayleigh-wave phase and splitting-function measurements for crustal thickness, surface topography and sea level height according to model CRUST2.0 (Bassin *et al.* 2000).
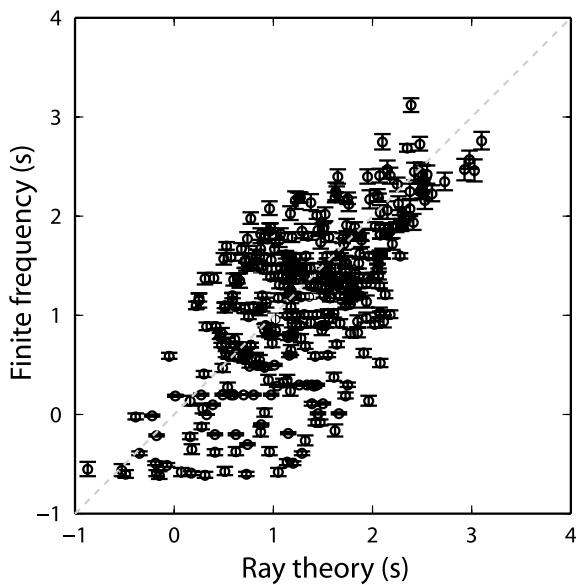
We used ray theory in RHW99 and RHW04 to determine crustal traveltime corrections. Here, we calculate the crustal corrections from normal-mode synthetics for the 1-D profiles of CRUST2.0 (Ritsema *et al.* 2009). These corrections better represent the nonlinear effects of the thin crust on seismic waves since propagation times are only a fraction of the relatively long ($T > 15$ s) wave period. Fig. 5 compares the one-way traveltime of shear waves through the crust according to ray theory and measurements using synthetic waveforms. It is evident that ray-theoretical and finite-frequency crustal traveltimes may differ by more than a second. For profile A0 of CRUST2.0, which is the 1-D profile for the oceanic crust excluding ridge and continental shelve regions, the ray theoretical shear wave crustal correction is -0.87 s while it is -0.55 s for a S wave with a period of 20 s. The difference of 0.3 s may not appear significant for a single shear-wave segment through the crust. However, the difference is more than a second for a *SSS* wave with two surface reflections within the oceans. This is substantial compared to the average traveltime delays.

3.4 Parametrization

We use the same spline functions as in RHW04 to parametrize vertical variation of shear velocity. The separation of the spline functions increases with depth. Relatively dense spline distribution helps to accommodate strong vertical shear-velocity variations across the lithosphere–asthenosphere boundary and the phase transition in the

finite-frequency   ray   difference

Figure 4. Phase velocity maps of fundamental mode Rayleigh waves at (top) 100 s and (bottom) 50 s periods. The left column shows the maps using finite-frequency kernels following Spetzler *et al.* (2002), the middle column shows the maps derived using the great-circle approximation, and the right column shows the difference. The maps have been parametrized using spherical harmonics up to degree 60.

Figure 5. Ray-theoretical (x-axis) and 'finite-frequency' (y-axis) one-way shear-wave traveltimes through the crust determined for the 360 crustal profiles from CRUST2.0 (Bassin *et al.* 2000). The finite-frequency traveltimes are determined by cross-correlating normal-mode synthetics for PREM and CRUST2.0 synthetics following Ritsema *et al.* (2009).

transition zone albeit at the expense of the vertical resolution at the base of the mantle. We parametrize horizontal variation of δV_S using spherical harmonics up to order 40.

4   MODEL S40RTS

The linear relationships between shear-velocity perturbations (**m**) and the traveltime, phase velocity and splitting measurements (**d**) can be written in matrix form:

$$\mathbf{d} = \mathbf{Gm}. \tag{1}$$

We estimate **m** by damped least-squares inversion (Tarantola 1987; Menke 1989) in which we minimise the misfit $(\mathbf{Gm} - \mathbf{d})^T(\mathbf{Gm} - \mathbf{d})/\mathbf{d}^T\mathbf{d}$ and the model norm $\epsilon\mathbf{m}^T\mathbf{m}$, weighted by the dampings factor ϵ. The solution to (1) is

$$\mathbf{m}^\dagger = \mathbf{G}^\dagger \mathbf{d}, \tag{2}$$

where $\mathbf{G}^\dagger$ is the generalized inverse of **G**. If $\mathbf{U}\Lambda\mathbf{U}^T$ is the eigen decomposition of $\mathbf{G}^T\mathbf{G}$, the generalised inverse is

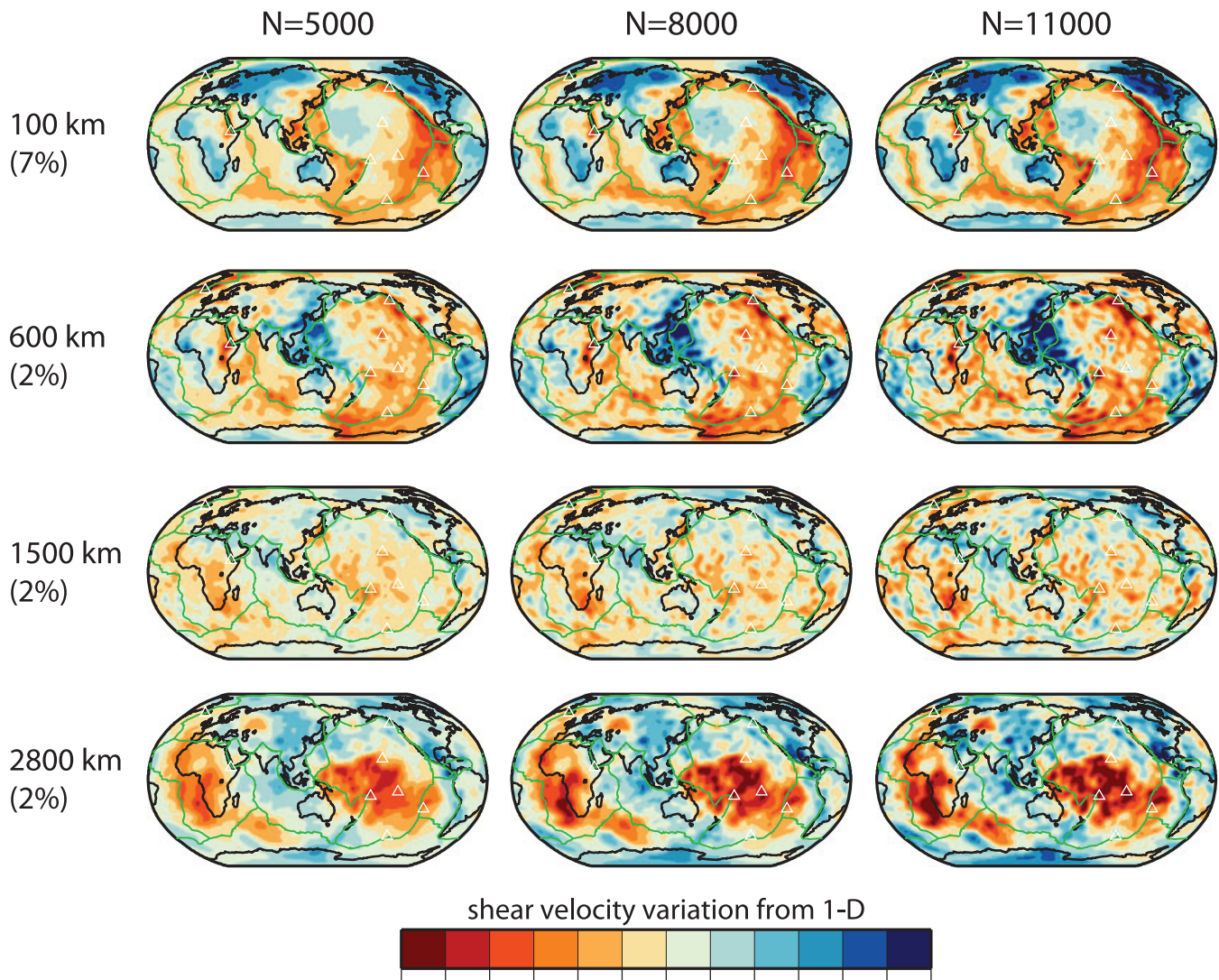$$\mathbf{G}^\dagger = \mathbf{U}\Lambda^{-1}\mathbf{U}^T\mathbf{G}^T, \tag{3}$$

where $\Lambda^{-1} = (\Lambda + \epsilon I)^{-1}$. Combining (1) and (2) yields

$$\mathbf{m}^\dagger = \mathcal{R}\,\mathbf{m}^t, \tag{4}$$

where $\mathcal{R} = \mathbf{G}^\dagger\mathbf{G}$ is the model resolution operator. The effective number of unknowns N of model $\mathbf{m}^\dagger$ is given by the trace of $\mathcal{R}$:

$$N = \text{trace}(\mathcal{R}). \tag{5}$$

Since we compute the eigen decomposition of $\mathbf{G}^T\mathbf{G}$, it is straightforward to determine models $\mathbf{m}^\dagger$ for any damping factor ϵ. A model $\mathbf{m}^\dagger$ that is damped strongly (i.e. ϵ is large) is characterised by relatively few effective unknowns N and it has small shear-velocity variations especially at the shortest scales. Fig. 6 shows shear-velocity heterogeneity for values of N of 5000, 8000 and 11 000. As N decreases (e.g. the damping factor ϵ increases), shear-velocity variations decrease. For example, the peak-to-peak shear-velocity variation at 2800 km depth is 4.7 per cent when $N = 8000$ but it drops to 3.4 per cent for $N = 5000$. The effect of damping is also evident from the amplitude spectra as a function of depth of these models (Fig. 7). While each model is characterised by a predominantly 'red' spectrum in the uppermost and lowermost mantle, an attribute that has been observed since the first tomographic images have been constructed (e.g. Su & Dziewonski 1991; Dziewonski *et al.* 2010), the decrease in spectral amplitude is strongest for the highest harmonic degrees (i.e. shortest wavelengths). This demonstrates that the smallest wavelength structures are the poorest constrained components of S40RTS.

Figure 6. Maps of shear-velocity heterogeneity at, from top to bottom, 100 km, 600 km, 1500 km and 2800 km depth for, from left to right, a total number of unknowns equal to $N = 5000$, $N = 8000$ and $N = 11\,000$ (eq. 5). Model S40RTS has 8000 unknowns.

Typically, N is estimated from misfit curves and by cross-validation (Hastie & Tibshirani 1990). Fig. 8 illustrates how model misfit varies as a function of N. Shown is the misfit of fundamental-mode and overtone Rayleigh waves at a period of 62 s (Fig. 8a), the traveltimes of S, SS, ScS and SKS (Fig. 8b), and the combined splitting functions (Fig. 8c). As expected, misfit decreases when N increases. The misfit is lowest for the fundamental mode Rayleigh wave which propagates through the strongly heterogeneous crust and uppermost mantle with well-resolved long-wavelength velocity heterogeneity. Misfit curves for phase delays for Rayleigh waves at other periods and the traveltimes of other body-wave phases have similar behaviour. For each data type, the decline in misfit is relatively small when N is larger than 8000.
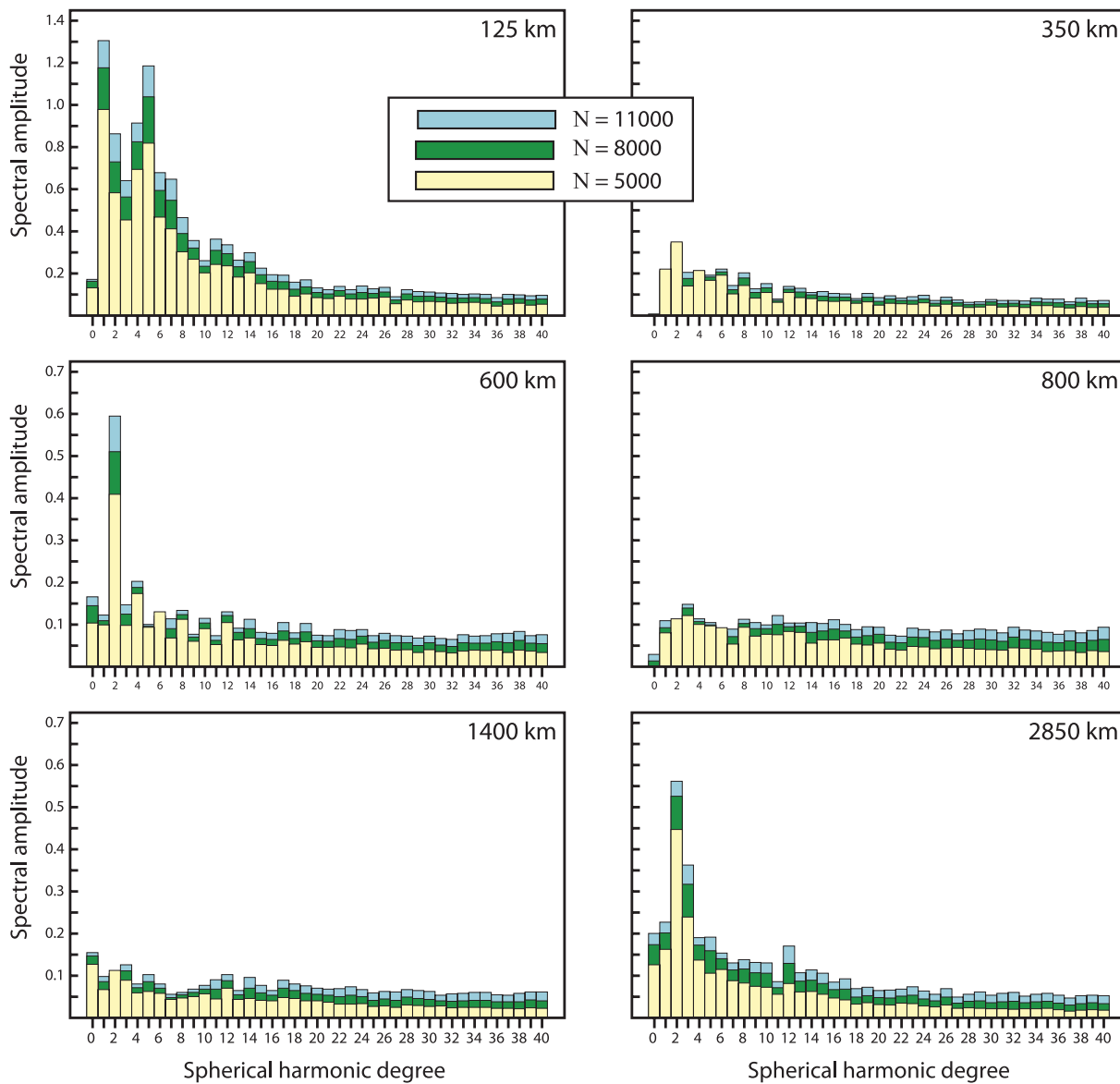
Selecting N is, to large extent, subjective since we do not fully understand the measurement errors, the systematic errors originating from unmodelled crustal effects and the effects of theoretical simplifications. Ideally, model uncertainties are evaluated by the analysis of 3-D synthetics (Komatitsch *et al.* 2002; Qin *et al.* 2009; Bozdağ & Trampert 2010). On the basis of the misfit curves of Fig. 8 and inspection of maps and cross sections we adopt S40RTS as the model with $N = 8000$ effective unknowns but we emphasize

that the misfit varies little for models with N between 5000 and 11 000.

4.1 Model images

Since S20RTS and S40RTS are based on the same data types and modelling approaches, it is not surprising that they correlate extremely well. Many of the model characteristics of S20RTS that we have discussed previously are still present in S40RTS. Although differences between S20RTS and S40RTS are subtle, they may have important implications for model interpretations.

Fig. 9 shows images of the upper mantle beneath the Atlantic and surrounding regions. Low velocity anomalies beneath the Mid-Atlantic Ridge, the Red Sea and East African Rift are narrower in S40RTS since lateral resolution is higher. The low-velocity anomaly beneath Iceland extends much deeper than elsewhere along the Mid-Atlantic Ridge (Montagner & Ritsema 2001) but it does not extend below the 660-km discontinuity. In S40RTS, this anomaly is significantly stronger (>3 per cent) than in S20RTS and may inhibit a pure thermal explanation.
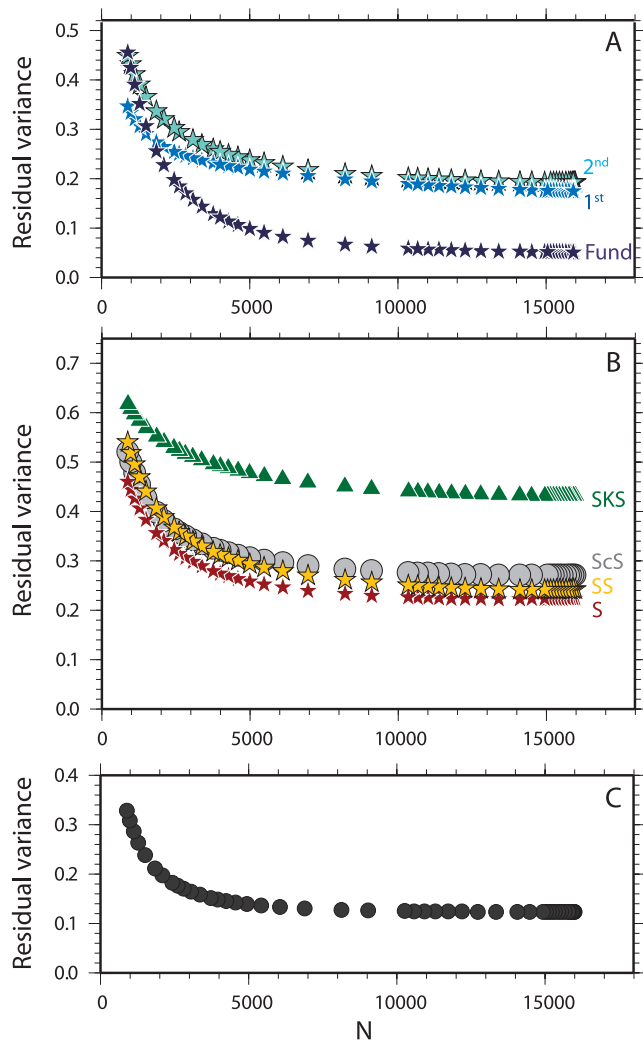
Figure 7. Spectra for six depths (125 km, 350 km, 600 km, 800 km, 1400 km and 2800 km) for models with (blue) $N = 11\,000$, (green) $N = 8000$ and (yellow) $N = 5000$. Note that the models with the fewest number of unknowns have the lowest amplitudes (as expected for damped inversions) and the strongest spectral decay which indicates that the shortest wavelength structures are the least resolved.

Shear velocities are relatively high in the upper mantle beneath the central Atlantic and along the Altantic coasts of South America and Africa. We have previously associated these high-velocity anomalies with the Central Atlantic Minimum, a thermal anomaly proposed by Bonatti (1996) and with small-scale convection due to contrasting thickness of the continental and oceanic lithosphere (King & Ritsema 2000; Ritsema *et al.* 2004). In addition, the velocity anomaly linked to the West African Craton is significantly weaker in S40RTS.

The change in the pattern of shear-velocity variation across the 660-km discontinuity is much stronger in S40RTS. This change is obvious in the spectra of Fig. 7 and the maps of Fig. 9 illustrate that this is not confined to the subduction zone regions. The profound change of shear-velocity heterogeneity across the 660 km depth was previously reported by Gu *et al.* (2001) and Ritsema *et al.* (2004). It indicates that the 660-km boundary marks a change in seismic velocity heterogeneity between the upper and lower mantle.
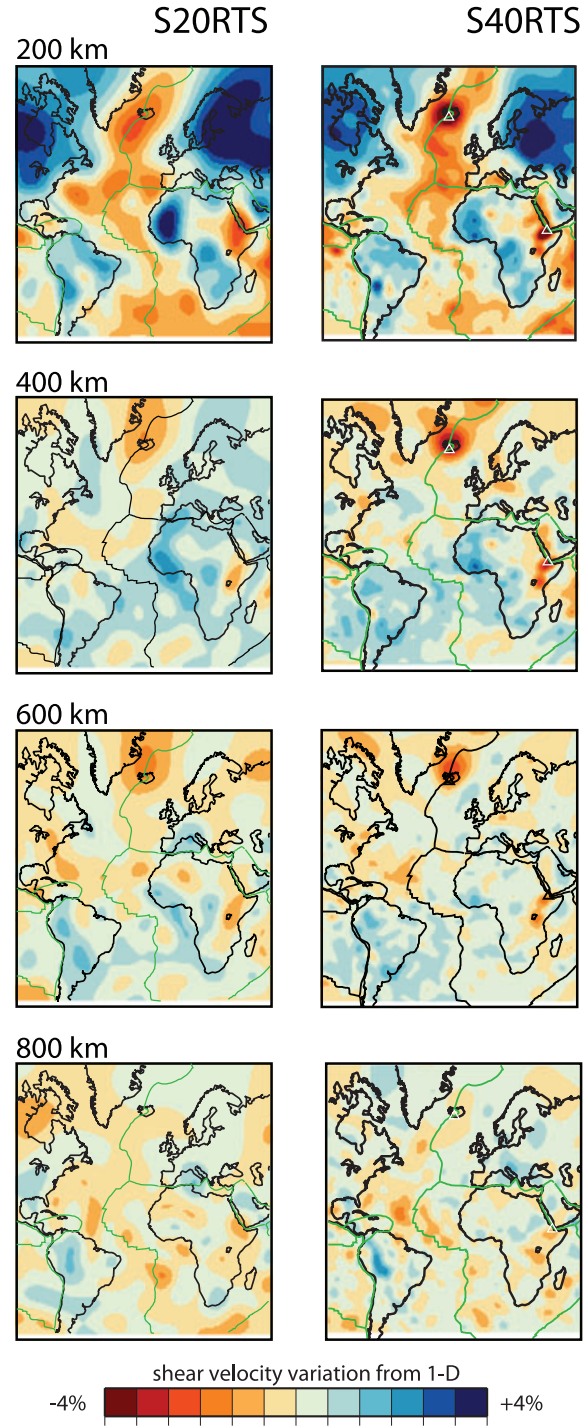
Whole-mantle cross-sections in Fig. 10(a) show large-scale structure in the deep mantle beneath Africa and Asia. The African anomaly extends through the lower mantle in S20RTS and S40RTS but it is less obvious from S40RTS that this anomaly connects with the East African Rift anomaly in the upper mantle as Ritsema *et al.* (1999) speculated. The relatively 'sharp' top of the African anomaly is consistent with rapid traveltime variations (Ritsema *et al.* 1998) and wave multi-pathing (Ni *et al.* 2002) as seen in regional network data. Fig. 10(b) shows a cross-section through the Western Pacific through S20RTS and S40RTS. Here, S40RTS present clear indication of slab accumulation above the 660-km discontinuity and a more pronounced contrast of shear velocity heterogeneity across the 660-km discontinuity. A continuation of the subducting slab beneath Japan into the lower mantle is less obvious in S40RTS even though velocity heterogeneity in the lower mantle is generally better resolved and stronger than in S20RTS.

Figure 8. Misfit as a function of *N* for subsets of the data. (a) phase delays of the fundamental-mode, the 1st, and 2nd Rayleigh wave overtone at a period of 62 s, (b) traveltime delays of *S, SS, ScS,* and *SKS*, (c) splitting functions.
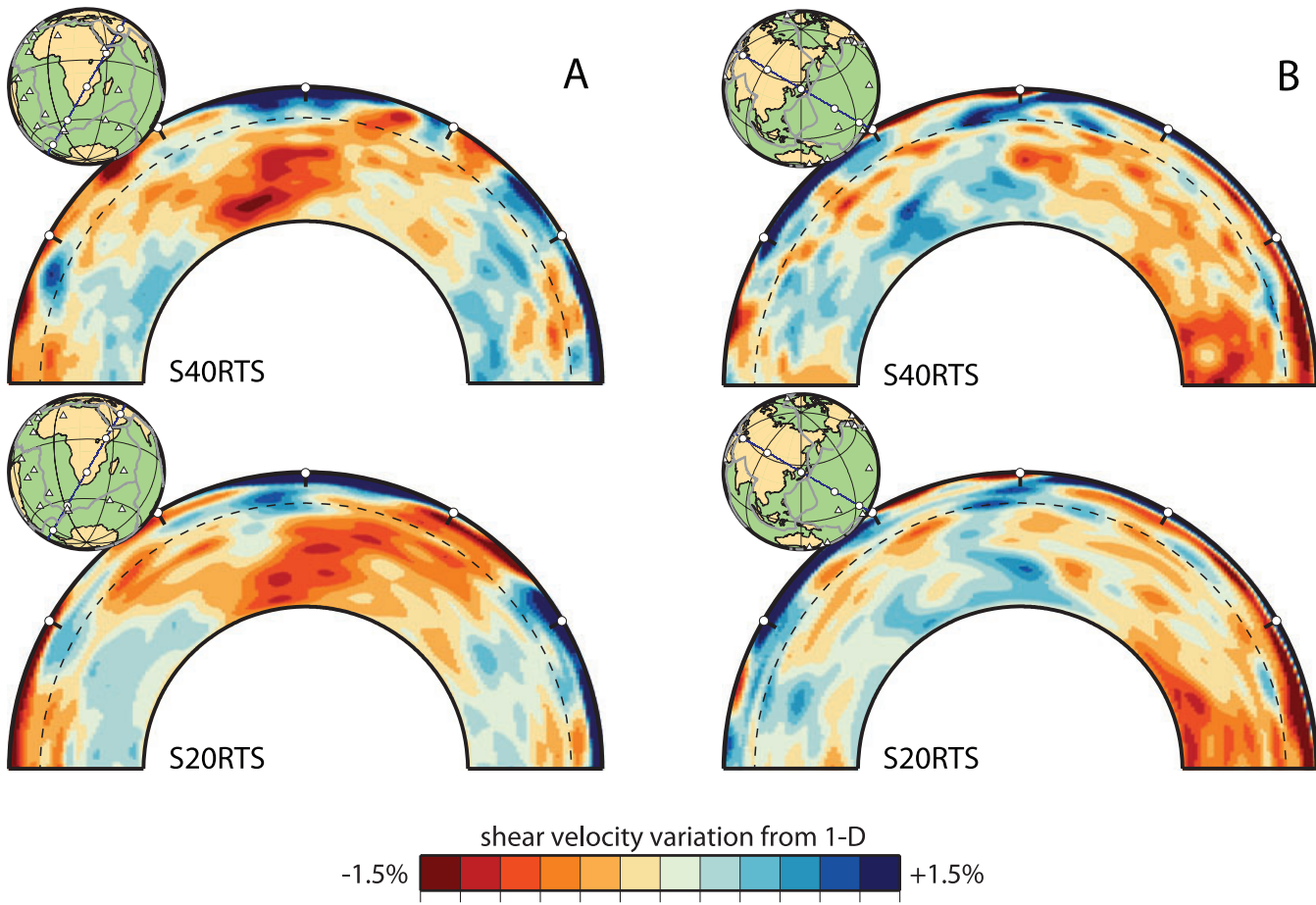
5 COMPARISON WITH OTHER MODELS

Fig. 11 (see also Fig. 1) compares S40RTS to other recently published shear-velocity models that are based on different data sets and modeling approaches: S362ANI (Kustowski *et al.* 2008), SAW642AN (Panning & Romanowicz 2006), TX2008 (Simmons *et al.* 2009) and HMSL-S (Houser *et al.* 2008). Model S362ANI is a whole-mantle shear-velocity model derived from surface-wave dispersion, mantle and body-wave waveforms and body-wave traveltimes. The data are inverted for isotropic (Voigt average) shear velocity and variations in shear-velocity anisotropy in the upper mantle. The authors also invert for a new 1-D reference model for shear and compressional velocity and anisotropy in the upper mantle. Model SAW642AN is a whole-mantle anisotropic model of the mantle derived from three-component surface-wave and body-wave waveforms. In contrast to all other models that are based on ray methods, SAW642AN is based finite-frequency kernels computed using the non-linear asymptotic coupling theory of Li & Romanowicz (1995). The data are inverted for isotropic (Voigt av-

Figure 9. Maps of shear-velocity heterogeneity at (from top to bottom) 200 km, 400 km, 600 km and 800 km depth beneath the Atlantic Ocean and surrounding regions. Shear-velocity perturbations are between −4 per cent and +4 per cent from the average value at each depth. Maps for model S20RTS are shown on the left and maps for model S40RTS are shown on the right.

erage) shear velocity and the parameter η that represents the ratio of horizontally and vertically polarized shear wave speed. Model TX2008 is the seismic component of a joint seismic/geodynamic inversion. The shear-velocity structure is derived from 46 000

Figure 10. Whole-mantle cross-sections centered on (A) eastern Africa and (B) the western Pacific for models (top) S40RTS and (bottom) S20RTS. Shear-velocity perturbations are between −1.5 per cent and +1.5 per cent.

shear-wave traveltimes but surface wave data have not been included. Model HMSL-S is derived from *S, SS, SS-S, ScS-S* traveltimes and Love and Rayleigh waves.

The models correlate best in the uppermost mantle. Here, shear-velocity anomalies are relatively large (>15 per cent) and broad (>5000 km) and, hence, impart large delays in fundamental-mode surface waves and multiple *S* wave reflections. Although less clear for HMSL-S, shear-velocity heterogeneity is associated with thermal anomalies due to plate tectonics and the presence of stable continents. The lowest shear velocities are resolved beneath the fast-spreading East Pacific Rise and velocities increase with increasing plate age. Highest shear velocities are resolved beneath the oldest regions of continents.

The core–mantle boundary region is also a region with relatively strong (>4 per cent), long-wavelength variations in shear velocity. This region is constrained by normal-mode splitting and the traveltimes of diffracted *S* waves, *ScS* and *SKS*. Absolute and differential (e.g. *ScS-S* and *S-SKS*) traveltime delays can exceed 15 s, especially for paths crossing the lower mantle beneath the central Pacific and Africa. Since all of the models shown in Fig. 11 are based on traveltime sets that include *S, ScS* and *SKS* it is not surprising that the core–mantle boundary maps are similar.

Each of the models, apart from HMSL-S, indicates that there is a significant contrast between shear-velocity structure at 600 km and 800 km depth. The high-velocity structure beneath the western Pacific region, associated with subduction, is one of the most
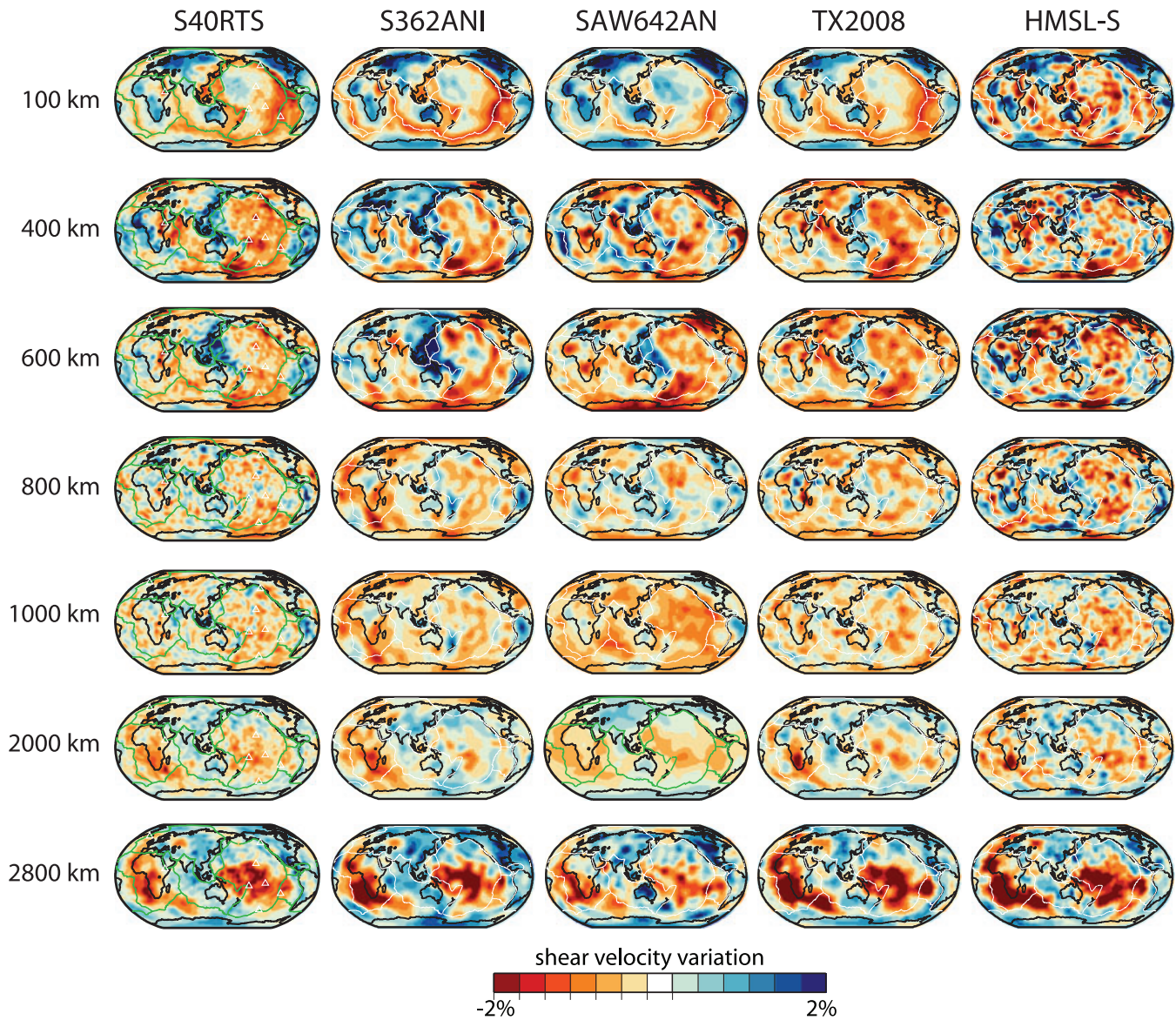
prominent structures just above the 660-km phase transition but not beneath the 660-km phase transition.

The differences between the models of Fig. 11 are in general larger than the differences between S20RTS and S40RTS. For example, models S40RTS and TX2008 present a contiguous low shear-velocity structure at 400 km depth beneath the Pacific Ocean at a depth of 400 km. This structure has a ring shape in models S362ANI and SAW642AN. Models S40RTS, SAW642AN, S362ANI and HMSL-S feature relatively high transition-zone velocities beneath the central Atlantic but these anomalies are missing in TX2008. The shear-velocity structure of SAW642AN at 400 km depth is anti-correlated from the structure at 100 km depth.

The model differences stem from differences in data sets and modelling approaches. Since teleseismic waves yield relatively poor sampling of the transition zone, its seismic resolution depends strongly on the modelling approaches (i.e. regularisation), on data coverage and whether overtone surface waves are analyzed as complete waveforms (e.g. S362ANI), as dispersion curves (e.g. S40RTS), or as triplicating, multiple *S* wave traveltimes (e.g. TX2008).

6 MODEL RESOLUTION

To explain model differences quantitatively, it is necessary to consider resolution tests that expose model inaccuracies. Here we show
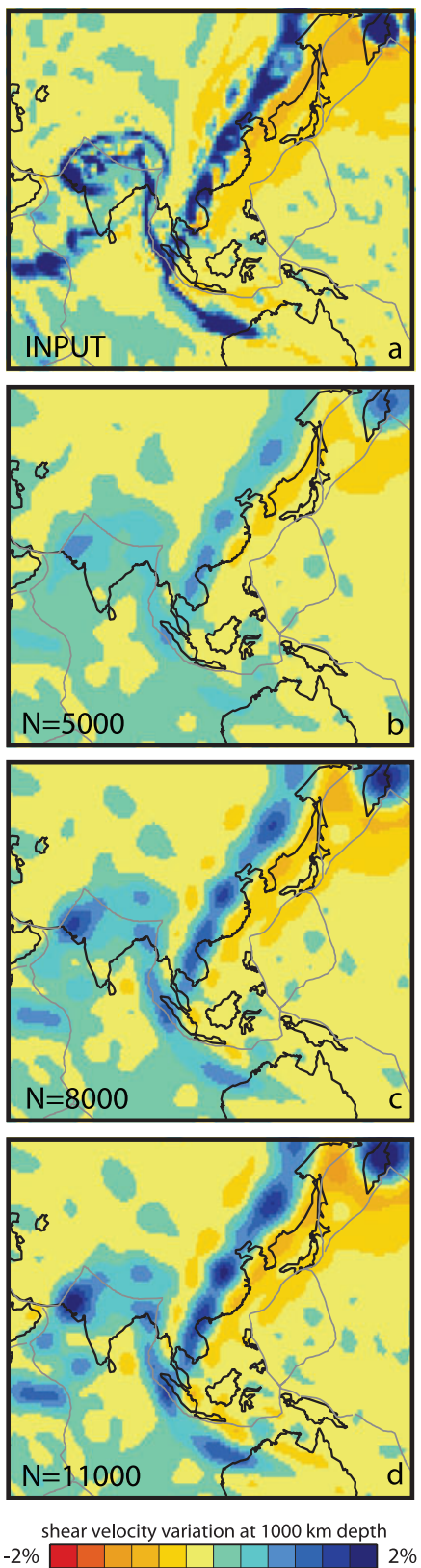
Figure 11. Comparison of shear-velocity maps at depths of (from top to bottom) 100 km, 400 km, 600 km, 800 km, 1000 km, 2000 km and 2800 km for model (from left to right) S40RTS, S362ANI (Kustowski *et al.* 2008), SAW642AN (Panning & Romanowicz 2006), TX2008 (Simmons *et al.* 2009) and HMSL-S (Houser *et al.* 2008). The velocity varies from −2 per cent to +2 per cent from the average value. Shear-velocity perturbations are between −7 per cent and +7 per cent from the average value for the map at 100 km depth.

an example of the 'checkerboard test' in which a hypothetical structure is projected into the model space of S40RTS and filtered using eq. (4): $\mathbf{m}^{OUT} = \mathcal{R}\mathbf{m}^{IN}$. As test structures one often invokes checkerboard patterns of alternating high and low velocity anomalies or isolated spikes. In Fig. 12, we consider a geophysical test structure $\mathbf{m}^{IN}$ determined by scaling the temperature variations in the mantle according to the numerical circulation model of Schuberth *et al.* (2009) into shear-velocity variations. Fig. 12(a) shows the shear-velocity variation for this model at a depth of a 1000 km. Figs 12(b), (c) and (d) shows the shear-velocity heterogeneity after filtering (i.e. $\mathbf{m}^{OUT}$) for $N = 5000$, 8000 and 11000. Most of the 'smearing' and de-amplification of the original structure is a result of the parametrization of S40RTS. Relatively narrow slabs are expanded into spherical harmonics up to degree 40 which can only accommodate structures with a wavelength of 1000 km

wavelength or more. Additional amplitude loss of the velocity variations is due the norm damping which increases with decreasing N.

A single test cannot provide a complete picture of the variable model resolution as discussed by Lévêque *et al.* (1993). However, the computation of Backus-Gilbert resolution kernels (e.g. Backus & Gilbert 1968) (see Ritsema *et al.* 2004, for examples) and tomographic filtering hypothesis tests for a wide variety of test structures can be readily performed using $\mathcal{R}$ for S40RTS. Insights into the heterogeneous resolution of S40RTS and artefacts in S40RTS images can therefore be gained from a large number of checkerboard tests without relying on a limited number of published examples. Several examples have been discussed by Ritsema *et al.* (2007), Bull *et al.* (2009), Downey & Gurnis (2009) and Schuberth *et al.* (2009).

The resolution matrix does not account for systematic errors in S40RTS due to, for example, theoretical simplifications, the

shear velocity variation at 1000 km depth

-2% 2%

Figure 12. Tomographic filtering experiment illustrating how (a) a hypothetical input structure (Schuberth *et al.* 2009) for the velocity variation at a depth of 1000 km is projected into S40RTS following Ritsema *et al.* (2007). In (b), (c), (d) the filtered model is calculated using equation (4) assuming 5000, 8000, and 11 000 unknowns, respectively.

effects of velocity anisotropy, or erroneous crustal corrections. However, $\mathcal{R}$ exposes inaccuracies of S40RTS due to model parametrization, damping and incomplete data coverage which are important factors limiting image resolution.

7 DISCUSSION AND CONCLUSIONS

Using a new compilation of Rayleigh-wave phase velocity, body-wave traveltime and normal-mode splitting function measurements, we have constructed a new model of the 3-D shear-velocity structure of the mantle. Although we employ similar data types than used for S20RTS, S40RTS is derived from an order-of-magnitude larger data set and it offers higher spatial resolution.

Since we compute the decomposition of $\mathbf{G}^T\mathbf{G}$, it is straightforward to compute models with different dampings factors and to quantify model resolution. We select S40RTS to be the model that has 8000 effective unknowns, as defined by the trace of the model resolution matrix, on the basis of data misfit and the visual inspection of maps and cross-sections. This choice is subjective since it is not straightforward to estimate measurement errors and to determine the effects of erroneous crustal corrections and theoretical simplifications. However, following equation (3) is it straightforward to estimate models for different values of ϵ (and hence a different number of unknowns N) and to determine the model resolution operator $\mathcal{R}$ as a function of damping ϵ.

Model interpretation is often focused on the continuity of slabs and the presence of plumes in the mantle. However, the tomographic models from Fig. 11 disagree even at scales much larger than subducting slabs and rising plumes, demonstrating that the seismic structure of the transition zone and lower mantle is still inconsistently imaged. Model differences stem from choices in data processing and modelling approaches. Software to make maps, cross-sections and surface rendering plots are useful when comparing competing seismic models. It is also key that published models are accompanied by utilities that enable quantitative estimates of resolution in order to develop meaningful geophysical interpretations.

REFERENCES

Backus, G.E. & Gilbert, J.F., 1968. The resolving power of gross earth data, *Geophys. J. R. astr. Soc.,* **16,** 169–205.

Bassin, C., Laske, G. & Masters, G., 2000. The current limits of resolution for surface wave tomography in North America, *EOS, Trans. Am. geophys. Un.,* **81,** F897.

Becker, T.W. & Boschi, L., 2002. A comparison of tomographic and geodynamic mantle models, *Geochem. Geophys. Geosys.,* **2,** 2001GC000171.

Bonatti, E., 1996. Anomalous opening of the Equatorial Atlantic due to an equatorial mantle thermal minimum, *Earth planet. Sci. Lett.,* **143,** 147–160.

Boschi, L., 2003. Measures of resolution in global body wave tomography, *Geophys. Res. Lett.,* **30**(19), doi:10.1029/2003GL018222.

Bozdağ, E. & Trampert, J., 2008. On crustal corrections in surface wave tomography, *Geophys. J. Int.,* **172,** 166–1082.

Bozdağ, E. & Trampert, J., 2010. Assessment of tomographic mantle models using spectral element seismograms, *Geophys. J. Int.,* **180,** 1187–1199.

Bull, A.L., McNamara, A.K. & Ritsema, J., 2009. Synthetic tomography of plume clusters and thermochemical piles, *Earth planet. Sci. Lett.,* **278,** 152–162.

Chen, P., Zhao, L. & Jordan, T.H., 2007. Full 3D tomography for the crustal structure of the Los Angeles region, *Bull. seism. Soc. Am.,* **97**(4), doi:10.1785/0120060222.

Dahlen, F.A., Hung, S.-H., Nolet, G. & Dahen, F.A., 2000. Freéchet kernels for fintie-frequency traveltimes – 1. Theory, *Geophys. J. Int.,* **141,** 157–174.

Debayle, E., Kennett, B. & Priestley, K., 2004. Global azimuthal seismic anisotropy and the unique plate-motion deformation of Australia, *Nature,* **433,** 509–512.

Deuss, A., Ritsema, J. & van Heijst, H.J., 2010. Splitting function measurements for Earth's gravest normal modes using recent large earthquakes, *Geophys. Res. Lett.,* p. in review.

Downey, N.J & Gurnis, M., 2009. Instantaneous dynamics of the cratonic Congo basin, *J. geophys. Res.,* **114**(B06401), doi:10.1029/2008JB006066.

Dziewonski, A.M. & Anderson, D.L., 1981. Preliminary Reference Earth Model, *Phys. Earth planet. Int.,* **25,** 297–356.

Dziewonski, A.M., Hager, B.H. & O'Connell, R.J., 1977. Large scale heterogeneity in the lower mantle, *J. geophys. Res.,* **82,** 239–255.

Dziewonski, A.M., Lekic, V. & Romanowicz, B.A., 2010. Mantle Anchor Structure: An argument for bottom up tectonics, *Earth planet. Sci. Lett.,* **299**(1–2), 69–79.

Ekström, G. & Dziewonski, A.M., 1998. The unique anisotropy of the Pacific upper mantle, *Nature,* **394,** 168–172.

Feirrera, A.M.G., Wodhouse, J.H., Visser, K. & Trampert, J., 2010. On the robustness of global radially anisotropc surface wave tomography, *J. geophys. Res.,* **115**(B04313), doi:10.1029/2009JB006716.

Fichtner, A., Kennett, B.L.N., Igel, H. & Bunge, H.-P., 2009. Full waveform tomography for upper-mantle structure in the Australasian region using adjoint methods, *Geophys. J. Int.,* **179**(3), 1703–1725.

Fukao, Y., Obayashi, M., Inoue, H. & Nenbai, M., 1992. Subducting slabs stagnant in the mantle transition zone, *J. geophys. Res.,* **97,** 4809–4822.

Gu, Y.J., Dziewonski, A.M., Su, W.-J. & Ekström, G., 2001. Models of the mantle shear velocity and discontinuities in the pattern of lateral heterogeneities, *J. geophys. Res.,* **106,** 11 169–11 199.

Hager, B.H. & Richards, M.A., 1989. Long-wavelength variations in Earth's geoid: physical models and dynamical implications, *Phil. Trans. R. Soc. Lond. A.,* **328,** 209–327.

Hager, B.H., Clayton, R.W., Richards, M.A., Comer, R.P. & Dziewonski, A.M., 1985. Lower mantle heterogeneity, dynamics topography and the geoid, *Nature,* **313,** 541–545.

Hastie, T.J. & Tibshirani, R.J., 1990. *Generalized Additive Models,* Chapman and Hall, London.

Houser, C., Masters, G., Shearer, P. & Laske, G., 2008. Shear and compressional velocity models of the mantle from cluster analysis of long-period waveforms., *Geophys. J. Int.,* **174,** 195–212.

King, S.D. & Ritsema, J., 2000. African hotspot volcanism: small-scale convection in the upper mantle beneath cratons, *Science,* **290,** 1137–1140.

Komatitsch, D., Ritsema, J. & Tromp, J., 2002. The spectral-element method, beowulf computing, and global seismology, *Science,* **298,** doi:10.1126/science.1076024.

Kustowski, B., Ekström, G. & Dziewonski, A.M., 2008. The anisotropic shear-wave velocity structure of the Earth's mantle, *J. geophys. Res.,* **1390,** doi:10.1029/2007JB005169.

Lévêque, J.J., Rivera, L. & Wittlinger, G., 1993. On the use of the checkerboard test to assess the resolution of tomographic inversions, *Geophys. J. Int.,* **115,** 313–318.

Li, X.D. & Romanowicz, B., 1995. Comparison of global wave-form inversions with and without considering cross-branch modal coupling, *Geophys. J. Int.,* **121,** 695–709.

Liu, Q. & Tromp, J., 2006. Finite-frequency kernels based on adjoint methods, *Bull. seism. Soc. Am.,* **96**(6), 2383–2397.

Liu, Q. & Tromp, J., 2008. Finite-frequency sensitivity kernels for global seismic wave propagation based upon adjoint methods, *Geophys. J. Int.,* **174**(1), 265–286.

Marquering, H., Snieder, R. & Nolet, G., 1996. Wave-form inversions and the significance of surface-wave mode coupling, *Geophys. J. Int.,* **124,** 258–278.

Menke, W., 1989. *Geophysical Data Analysis: Discrete Inverse Theory,* Academic Press Inc., San Diego.

Montagner, J.P., 1998. Where can seismic anisotropy be detected in the Earth's mantle? In boundary layers..., *Pure appl. Geophys.,* **151,** 223–256.

Montagner, J.P., 2007. Upper mantle structure: global isotropic and anisotropic tomography, in *Treatise on Geophysics,* vol.1, pp. 559–590, Elsevier, Amsterdam.

Montagner, J.-P. & Ritsema, J., 2001. Interactions between ridges and plumes, *Science,* **294,** 1472–1473.

Montelli, R., Nolet, G., Masters, G., Dahlen, F.A. & Hung, S.-H., 2004. Global P and PP traveltime tomography: rays versus waves, *Geophys. J. Int.,* **158,** 637–654.

Montelli, R., Nolet, G. & Dahlen, F.A., 2006. Comment on 'Banana-doughnut kernels and mantle tomography' by van der Hilst and de Hoop, *Geophys. J. Int.,* **167,** 1204–1210.

Ni, S., Tan, E., Gurnis, M., Helmberger, D.V. & Crotwell, H.P., 2002. Sharp sides to the African superplume, *Science,* **296**(5574), 1850–1852.

Nolet, G. & Dahen, F.A., 2000. Wave front healing and the evolution of seismic delay times, *J. geophys. Res.,* **105,** 19 043–19 054.

Panning, M. & Romanowicz, B., 2006. A three dimensional radially anisotropic model of shear velocity in the whole mantle, *Geophys. J. Int.,* **167,** doi:10.1111/j.1365-246X.2006.03100.x.

Qin, Y., Capdeville, Y., Montagner, J.-P., Boschi, L. & Becker, T.W., 2009. Reliability of mantle tomography models assessed by spectral element simulation, *Geophys. J. Int.,* **177,** 125–144.

Resovsky, J.S. & Ritzwoller, M.H., 1999. A degree 8 mantle shear velocity model from normal mode observations below 3 mHz, *J. geophys. Res.,* **104,** 993–1014.

Ricard, Y., Richards, M.A., Lithgow-Bertelloni, C. & LeStunff, Y., 1993. A geodynamic model of mantle density heterogeneity, *J. geophys. Res.,* **98**(B12), 21 895–21 909.

Richards, M.R. & Engebretson, D.C., 1992. Large-scale mantle convection and the history of subduction, *Nature,* **355,** 437–440.

Ritsema, J. & van Heijst, H.J., 2002. Constraints on the correlation of P- and S-wave velocity heterogeneity in the mantle from P, PP, PPP, and PKPab traveltimes, *Geophys. J. Int.,* **149,** 482–489.

Ritsema, J., Ni, S., Helmberger, D.V. & Crotwell, H.P., 1998. Anomalous shear velocity reductions and gradients in the lower mantle beneath Africa, *Geophys. Res. Lett.,* **25,** 4245–4248.

Ritsema, J., van Heijst, H.J. & Woodhouse, J.H., 1999. Complex shear velocity structure imaged beneath Africa and Iceland, *Science,* **286,** 1925–1928.

Ritsema, J., van Heijst, H.J. & Woodhouse, J.H., 2004. Global transition zone tomography, *J. geophys. Res.,* **109,** doi:10.1029/2003JB002610.

Ritsema, J., McNamara, A.K. & Bull, A.L., 2007. Tomographic filtering of geodynamic models: implications for model interpretation and large-scale mantle structure, *J. geophys. Res.,* **112**(B01303), doi:10.1029/2006JB004566.

Ritsema, J., van Heijst, H.J., Woodhouse, J.H. & Deuss, A., 2009. Long-period body wave traveltimes through the crust: implication for crustal corrections and seismic tomography, *Geophys. J. Int.,* **179,** 1255–1261.

Romanowicz, B., 2003. Global mantle tomography: progress status in the last 10 years, *Annu. Rev. Geoph. Space Phys.,* **31**(1), 303–328.

Schuberth, B.S.A., Bunge, H.-P. & Ritsema, J., 2009. Tomographic filtering of high-resolution mantle circulation models: can seismic heterogeneity be explained by temperature alone?, *Geochem. Geophys. Geosyst.,* **10,** doi:10.1029/2009GC002401.

Sigloch, K., McQuarrie, N. & Nolet, G., 2008. Two-stage subduction history under North America inferred from multiple-frequency tomography, *Nature Geosci.,* **1,** doi:10.1038/ngeo231.

Simmons, N.A., Forte, A.M. & Grand, S.P., 2009. Joint seismic, geodynamic and mineral physical constraints on three-dimensional mantle

heterogeneity: implications for the relative importance of thermal versus compositional heterogeneity, *Geophys. J. Int.,* **177,** 1284–1304.

Simons, F.J., Nolet, G., Georgief, P., Babcock, J.M., Regier, L.A. & Davis, R.E., 2009. On the potential of recording earthquakes for global seismic tomography by low-cost autonomous instruments in the oceans, *J. geophys. Res.,* **114**(B05307), doi:10.1029/2008JB006088.

Spetzler, J., Trampert, J. & Snieder, R., 2002. The effect of scattering in surface wave tomography, *Geophys. J. Int.,* **149,** 755–767.

Su, W.J. & Dziewonski, A.M., 1991. Predominance of long-wavelength heterogeneity in the mantle, *Nature,* **352,** 121–126.

Tape, C., Liu, Q., Maggi, A. & Tromp, J., 2009. Adjoint Tomography of the Southern California Crust, *Science,* **325**(5943), 988–992.

Tarantola, A., 1987. *Inverse Problem Theory,* Elsevier, Amstedam.

Trampert, J. & Spetzler, J., 2006. Surface wave tomography: finite-frequency effects lost in the null space, *Geophys. J. Int.,* **164,** 394–400.

Trampert, J. & van Heijst, H.J., 2002. Global azimuthal anisotropy in the transition zone, *Science,* **296,** 1297–1299.

van der Hilst, R.D. & de Hoop, M.V., 2005. Banana-doughnut kernels and mantle tomography, *Geophys. J. Int.,* **163,** 956–961.

van der Hilst, R.D., Engdahl, R., Spakman, W. & Nolet, G., 1991. Tomographic imaging of subducted lithosphere below Northwest Pacific island arcs, *Nature,* **353,** 37–43.

van Heijst, H.J. & Woodhouse, J.H., 1997. Measuring surface-wave overtone phase velocities using a mode branch stripping technique, *Geophys. J. Int.,* **131,** 209–230.

van Heijst, H.J. & Woodhouse, J.H., 1999. Global high-resolution phase velocity distributions of overtone and fundamental-modesurface waves determined by mode branch stripping, *Geophys. J. Int.,* **137,** 601–620.

Wessel, P. & Smith, W.H.F., 1995. New version of the Generic Mapping Tools released, *EOS, Trans. Am. geophys. Un.,* **76,** 329.

Woodhouse, J.H. & Dziewonski, A.M., 1984. Mapping the upper mantle: three dimensional modeling of Earth structure by inversion of seismic waveforms, *J. geophys. Res.,* **89,** 5953–5986.

Woodhouse, J.H., Giardini, D. & Li, X.D., 1986. Evidence for inner core anisotropy from free oscillations, *Geophys. Res. Lett.,* **13,** 1549–1552.

Wysession, M.E., 1996. How well do we utilize global seismicity?, *Bull. seism. Soc. Am.,* **86,** 1207–1219.

Yoshizawa, K. & Kennett, B.L.N., 2002. Non-linear waveform inversion for surface waves with a neighbourhood algorithm – application to multimode dispersion measurements, *Geophys. J. Int.,* **149,** 118–133.

Zaroli, C., Debayle, E. & Sambridge, M., 2010. A global dataset of frequency dependent body wave travel times, *Geophys. J. Int.,* **182**(2), 1,025–1,042.

Zhao, L., Jordan, T.H. & Chapman, C.H., 2000. Three-dimensional Fréchet differential kernels for seismic delay times, *Geophys. J. Int.,* **141,** 558–576.